Biological fingerprint using scout computed tomographic images for positive patient identification

First author (corresponding author)
Name: Yasuyuki Ueda
Institution:
Division of Health Sciences, Graduate School of Medicine, Osaka University
E-mail: ueda@sahs.med.osaka-u.ac.jp
Work telephone number: +81-6-6879-2443
Work fax number: none
Postal address: 1-7 Yamadaoka, Suita, Osaka 565-0871, Japan

Second author
Name: Junji Morishita
Institution:
Department of Health Sciences, Faculty of Medical Sciences, Kyushu University
E-mail: junjim@med.kyushu-u.ac.jp
Work telephone number: +81- 92-642-6673
Work fax number: none
Postal address: 3-1-1, Maidashi, Higashi-ku, Fukuoka 812-8582, Japan

Third author
Name: Tadashi Hongyo
Institution:
Division of Health Sciences, Graduate School of Medicine, Osaka University
E-mail: hongyo@sahs.med.osaka-u.ac.jp
Work telephone number: +81-6- 6879-2562
Work fax number: none
Postal address: 1-7 Yamadaoka, Suita, Osaka 565-0871, Japan

Abstract

Purpose: Management of patient identification is an important issue that should be addressed to ensure patient safety while using modern healthcare systems. Patient identification errors can be mainly attributed to human errors or system problems. An error-tolerant system, such as a biometric system, should be able to prevent or mitigate potential misidentification occurrences. Herein, we propose the use of scout computed tomography (CT) images for biometric patient identity verification and present the quantitative accuracy outcomes of using this technique in a clinical setting.

Methods: Scout CT images acquired from routine examinations of the chest, abdomen, and pelvis were used as biological fingerprints. We evaluated the resemblance of the follow-up with the baseline image by comparing the estimates of the image characteristics using local feature extraction and matching algorithms. The verification performance was evaluated according to the receiver operating characteristic (ROC) curves, area under the ROC curves (AUC), and equal error rates (EER). The closed-set identification performance was evaluated according to the cumulative match characteristic curves and rank-one identification rates (R1).

Results: A total of 619 (383 males, 236 females, age range 21–92 years) patients who

underwent baseline and follow-up chest-abdomen-pelvis CT scans on the same CT system were analyzed for verification and closed-set identification. The highest performances of AUC, EER, and R1 were 0.998, 1.22%, and 99.7%, respectively, in the considered evaluation range. Furthermore, to determine whether the performance decreased in the presence of metal artifacts, the patients were classified into two groups, namely scout images with (255 patients) and without (364 patients) metal artifacts, and the significance test was performed for two ROC curves using the unpaired Delong's test. No significant differences were found between the ROC performances in the presence and absence of metal artifacts when using a sufficient number of local features. Our proposed technique demonstrated that the performance was comparable to that of conventional biometrics methods when using chest, abdomen, and pelvis scout CT images. Thus, this method has the potential to discover inadequate patient information using the available chest, abdomen, and pelvis scout CT image; moreover, it can be applied widely to routine adult CT scans where no significant body structure effects due to illness or aging are present.

Conclusions: Our proposed method can obtain accurate patient information available at the point-of-care and help healthcare providers verify whether a

patient's identity is matched accurately. We believe the method to be a key solution for patient misidentification problems.

Keywords:

Biological fingerprint, Biometrics, Patient verification, Computed tomography, Scout image

1. Introduction

A patient's identity should be verified prior to clinical examinations or treatments to ensure that the correct patient undergoes all the relevant medical practices [1-5]. Many hospitals rely on manual processes and name tags, such as a wristband with a barcode, to identify patients during registration [2-5]. Identification procedures, such as the use of at least two patient identifiers are often adopted (e.g., name and date of birth); however, these confirmations are not always foolproof [1-5]. Healthcare providers may struggle to collect precise patient information and match individuals to their medical records. There are several human factors that can cause patient misidentification, including communication or human errors in healthcare work [6]. While human error is innate in our nature, some human errors can be avoided [6]. Healthcare providers can practice patient confirmation processes to ensure that they are examining the correct patient. However, this may increase their workloads. In addition to conventional patient confirmation, to use of biometrics for automated patient identity verification can be expected to reduce patient misidentification problems [7].

The term biometrics refers to the use of behavioral and biological characteristics to identify an individual [8-27]. Biometrics are utilized as a part of either a verification

or an identification system [11-27]. Biometric verification refers to the authentication of a patient's identity by comparing a biological fingerprint with one pre-stored in a database [8-10]. Patient verification is a crucial means to ascertain the correctness of a patient's identity. Biometric verification process for healthcare authenticates a patient's identity in addition to the manual checking conducted by healthcare providers [11-15]. Biometric identification usually refers to the closed-set identification of someone whose biological fingerprint is stored in a database [8-10]. Patient identification is a crucial means to identify unconscious or unknown patients [25-27].

We have previously reported on the usefulness of biological fingerprints using scout magnetic resonance (MR) images of the brain [11]. In other previous studies, medical image biometrics were reported using chest [19-22, 25-27] and knee [23] X-ray images, optical surface images [13], and patient X-ray images [24] acquired during a radiotherapy set-up process, facial images[15] extracted from computed tomography (CT), and facial images[12, 14] acquired with mobile camera. Biometrics for healthcare preferred to be a simple process to enable identity verification under various patient conditions [1-5]. Furthermore, although additional biometric input devices were used to acquire and process patient characteristics in some studies [12-14], it is desirable to avoid such additional devices for appropriate

handling of private information.

Biological fingerprint techniques using scout images have high versatility for verifying a patient's identity [11]. Scout images are preliminary image sets that are routinely obtained for localization to determine ranges in CT or MR imaging examinations. Consequently, it is possible to verify the identity of a patient using only some existing scout images. Therefore, there is no need to separately scan a patient to obtain characteristic data for biometrics. Additionally, if we can set all the parameters required for biometrics in advance, the verification process can be executed automatically during a clinical imaging. Thus, use of scout image based biometrics makes the process convenient at both the healthcare provider side and patient side. However, this technique is not applicable to other imaging methods. Nevertheless, verification of the patient identity during CT examination as well as chest X-ray and head MR imaging examinations is important. We believe that a biological fingerprint technique can be used as a patient confirmation tool during frequently performed CT examinations. The purpose of our study is to a) use scout CT images from the chest, abdomen, and pelvis for patient identity verification during CT examinations to avoid performing a CT scan on the wrong patient, and b) present quantitatively accurate outcomes using this technique in a clinical setting.

2. Materials and Methods

2.1. Subjects:

This study was conducted as a retrospective, observational study and was approved by the Institutional Review Boards at Osaka University and Yamaguchi University Hospital. Written informed consent was not required owing to the retrospective design of this study. All procedures conducted herein were in conformance with the Declaration of Helsinki.

This study used the scan information from 619 patients who underwent two chest-abdomen-pelvis CT scans between May 2015 and May 2016 at the Yamaguchi University Hospital in Japan. Patients under the age of 20 years, those who have intravenous iodined contrast administration, and those who did not undergo the exams in the required supine position with their arms raised were excluded. All scout scans were performed using a CT system (SOMATOM Sensation 64, Siemens Medical Solutions, Forchheim, Germany). Furthermore, a preliminary study of different CT system models was performed for a patient who underwent three chest-abdomen-pelvis CT examinations, i.e., two baseline scans acquired using SOMATOM Sensation and Definition (both Siemens Medical Solutions, Forchheim, Germany) and a follow-up scan acquired using SOMATOM Sensation. **Error! Reference source not found.**

shows the patient characteristics of this study. **Error! Reference source not found.**

115 shows the scan parameters of the scout CT.

Figure 1 shows the scanning geometry of the chest-abdomen-pelvis scout CT scan.

2.2. Methodology:

2.2.1. Outline:

Figure 2 shows the flowchart for the biological fingerprint verification framework of our method. The procedure comprises four major steps, namely a) geometric correction, b) local feature extraction, c) valid correspondence evaluation, and d) similarity evaluation. Biological fingerprint processing was performed using MATLAB version R2018a (MathWorks Inc., 2018) on Windows 10.

2.2.2. Geometric correction

The projected patient transverse size of the scout CT image varies with the scanner table height owing to geometric effects. The geometric effects of changing the table height can be calculated using the method of similar triangles. The geometric correction factor at the height of the rotation center can be parameterized as follows:

$$\alpha = \frac{D_{So}}{D_{So} + TH},$$

where a denotes the magnification factor in the transverse direction, D_{so} denotes the distance from the focal spot in the X-ray tube to the rotation center, and the table height, TH, denotes the distance from the couch to the rotation center. Accordingly, all scout CT images are processed for correction to cancel this geometric error. Figure 3a shows the original follow-up scout CT image, and Fig. 3(b-d) shows the cropped processing area of the images after geometric correction.

2.2.3. Local feature extraction:

Each initial local feature point is used as the center for defining the corresponding square regions of interest (ROI) based on which the template images of the follow-up scout CT images are obtained. An initial local feature point algorithm [28] uses the following two steps. First, local maxima are computed using

the data in the follow-up scout image recorded only within the couch area. Specifically, the local maxima are the points that are strictly larger in value than all other pixels in a 3 × 3 neighborhood. The local maxima are then sorted in a descending order according to the peak value, and the coordinates of the first N local maxima are obtained as the initial local feature points.

We consider that validating the computational cost and performance depending on the number of the initial local feature points and template matrix sizes is necessary. Figures 3b, 3c, and 3d, show examples corresponding to N=100, 200, and 300, respectively, of the initial local feature point set. In addition, Figs 3f, 3g, and 3h, show examples of including metal artifact corresponding to N=100, 200, and 300, respectively, of the initial local feature point set.

2.2.4. Valid correspondence evaluation

Local corresponding points were computed using the template matching technique via normalized cross-correlation [30] between the follow-up and the baseline scout CT images. The template matching technique, which is a feature point tracking method, is used to identify the corresponding pairs linked to the initial local feature point set O in the follow-up scout CT image. A local corresponding point set P is thus obtained in the baseline scout CT image. Each local corresponding point set P is used as the center for a square ROI according to which the template images of the baseline scout CT image are obtained. The template matching technique is executed again to find the corresponding pairs linked to the local corresponding point set P in the baseline scout CT image. Accordingly, the final local feature point of the follow-up scout CT image O' is obtained.

2.2.5. Similarity evaluation

To examine the resemblance, we determined the correspondence rate, C, using the following equations:

$$\mathrm{C} = \frac{M}{N},$$

$$M = |Q|,$$

$$Q = (O \cap O'),$$

$N = |O|$.

Let M and N be the numbers of respective feature points Q and O. Additionally, let Q be the valid corresponding feature point that consists of all the elements in which the distance between O and O' is within two pixels. If the correspondence rate is less than the threshold value, the estimation of the follow-up and baseline scout CT images is identified as an impostor (different patient) pair. Otherwise, the estimations of the follow-up and baseline scout CT images are accepted as a genuine (same patient) pair.

2.3. Performance evaluation

The verification performance of our method was evaluated in terms of the receiver operating characteristic (ROC) curve and its corresponding equal error rates (EERs) and area under the ROC curves (AUCs). The EER on the ROC curve indicates the point that has an equal probability for the misclassification of the genuine- or impostor pairs. In a good biometric system, the EER should be as low as possible [28]. The unpaired DeLong's test [31, 32] was used to evaluate the AUCs between two groups classified as including (255 patients) or not including (364 patients) metal artifacts. In the ROC analysis, the number of impostor pairs was reduced by using random sampling to make the numbers of genuine and impostor pairs the same. P

values of < 0.05 were considered statistically significant. Statistical analysis was performed using the computing environment R version 3.6.0 (R Development Core Team, 2019) on Windows 10.

The closed-set identification performance of our method was evaluated in terms of the cumulative match characteristic (CMC) curve and its rank-one identification rate (R1). The true-positive identification rate is the proportion of correctly matched identifications contained within the top R matches, where R is the rank. [28] The CMC curve is used to evaluate the true-positive identification rate within the top R matches [28]. Thus, R1 indicates that the rank of the genuine patient pair is higher than that of all impostor patient pairs. The higher the value of R1 is, the better the biometric system is for closed-set identifications.

3. Results

Figure 4 shows scout CT image examples of genuine and impostor pair analyses. The correspondence rates achieved are 80.6% for the genuine pair and 18.0% for the impostor pair. The correspondence rate is a characteristic factor for distinguishing genuine matches from impostor matches. If each point correspondence is correct, all lines connecting each valid corresponding feature point should be parallel. Therefore, a non-parallel line connecting each valid corresponding feature point represents incorrect point correspondence. Thus, the correspondence rate is higher for genuine matches than it is for impostor matches. In addition,

Figure **5** shows an example of a scout CT image of an impostor pair comparison with a correspondence rate of 44.3%. The obtained result demonstrates the potential risk for misclassification of this dataset as a genuine pair (i.e., as a false acceptance case). Furthermore, Figure 6 shows low correspondence rate examples for a genuine pair evaluation due to a) patient's body posture translocations and b) a residual contrast medium in the gastrointestinal tract at a follow-up scan, where the correspondence rates were determined to be 15.0 and 33.3%, respectively. We believe that several intra-patient temporal changes such as physical abnormalities, body posture translocations, and metal artifacts may affect the performance of our

method. Figure 7 shows examples of scout CT images for analyses of same and different CT systems. The correspondence rates achieved are 58.7% for the same CT system and 61.0% for a different CT system. The correspondence rate for the same CT system had an average value of 65.4 ± 16.3% for 619 patients.

Figure **8** shows the ROC curves for an initial local feature point set size of 300; the template matrix size of 16 × 16 showed the most successful performance with an AUC of 0.998, and an EER of 1.22%. This was followed by the template matrix sizes of 32 × 32 (AUC of 0.997 and EER of 1.68%), and of 8 × 8 (AUC of 0.996 and EER of 1.62%). The template matrix size of 64 × 64 exhibited the poorest performance in the ROC analyses; nevertheless, our method achieved AUC and EER values of 0.989 and 3.77%, respectively. Figure 9 shows the CMC curves for an initial local feature point set size of 300; the template matrix size of 16 × 16 produced the most successful performance, in which R1 was 99.7%. This was followed by the template matrix sizes of 8 × 8 and 32 × 32, for which R1 was 99.0 %. The template matrix size of 64 × 64 gave the poorest performance in the CMC analyses; nevertheless, our method achieved R1 values of 95.6%.

Figure 10 shows a comparison of the performance values, where a) is the EER on

the verification performance and b) is the R1 on the closed-set identification performance at various numbers of initial local feature points (50 - 300) for the four template matrix sizes. For all template matrix sizes, as the number of initial local feature points increased, the EER decreased gradually, while the R1 increased gradually. The template matrix size of 16 × 16 yielded the best verification and closed-set identification performances among the four different template matrix sizes studied herein for different numbers of initial local feature points.

As shown in Figure 3a-3d, the unique image features used for the identification of individual patients in our method were mainly detected in the thoracic-lumbar spine, mediastinum, lung boundary, and pelvic brim regions. However, the local maxima employed as the initial local feature point may be concentrated on a high contrast part under a patient's scout CT image, and a metal artifact example is shown in Figure 3e-3h. The actual local feature extraction processes using the top-100, top-200, and top-300 peaks of the local maxima is shown in Figure 3f, 3g, and 3h, respectively. More specifically, in Figure 3f, the majority of the 100 initial local feature points appear to be concentrated on a specific gastrointestinal tract with residual contrast medium, in which it could be difficult to identify the individual patients. **Error! Reference source not found.** shows the AUCs and p values classified by whether the

scout CT image includes a metal artifact or not at the follow-up CT scan. Significant differences were observed between the ROC performances at 100 and 200 initial local feature points of the scout CT images with and without metal artifacts for the unpaired Delong's test ($p < 0.05$). However, there were no significant differences between the ROC performances at 300 initial local feature points of the scout CT images with and without metal artifacts for the unpaired Delong's test. We, therefore, believe that it is necessary to increase the number of initial local feature points in regard to a patient where metal artifacts are observed in the follow-up scout CT image as shown in Figure 6b. We note that our method of using 300 initial local feature points exhibits high performance levels both in the presence and absence of a metal artifact in the scout CT image.

4. Discussion

In this study, we have proposed a novel biological fingerprint technique using scout CT images from the chest, abdomen, and pelvis under a clinical setting. Our method is innovative because verification of the patient's identity is possible without using other biometric input devices if scout CT scan is acquired, and subjecting a wrong patient to CT scan can be avoided during CT examination.

The evaluations demonstrated the effectiveness of the proposed technique for the identification and verification of patients using scout CT images as the biological fingerprint. Our method achieved AUC, EER, and R1 values of 0.998, 1.22%, and 99.7%, respectively, for a template matrix size of 16 × 16 and 300 initial local feature points. In previous research by Shimizu et al. [20] and KAO et al. [22], the highest AUC values for biometric verifications from chest X-ray images were 0.994 and 0.963 ± 0.002, respectively. Furthermore, for biometrics based on scout MR images, Ueda et al. [11] achieved the highest AUC of 0.998, EER of 1.37%, and R1 of 98.6%. Thus, our method yielded identification and verification performances equivalent to the conventional methods.

Our result indicated that optimal parameter settings for the template matrix size and the number of initial local feature points are 16 × 16 and 300, respectively. We

considered that the optimal matrix size should be 16 × 16 because the patient's body posture on the couch changes slightly at each scan in a routine CT examination. As the cause of the performance degradation with template matrix sizes greater than or equal to 32 × 32, it is conceivable that a wider range of corresponding points was searched when the template matrix size was increased. Furthermore, a template matrix size of 8 × 8 is too small to be able to distinguish each patient's characteristics.

The performance of our method improved monotonically with increase in the number of initial local feature points. Furthermore, for the number of initial local feature points of 300 and template matrix size of 16 × 16, the AUC values with and without metal artifacts were 0.998 and 0.999, respectively, and hence there was no significant difference. However, on changing the number of initial local feature points to 200 or less, there were significant differences between the groups with and without metal artifacts ($P < 0.05$). The overall performance of our method may change when used for a database that contains data of patients from follow-up scan with various physical abnormalities, i.e., trauma, installed clinical metallic devices, and a contrasting medium included in the body. However, we considered that the results obtained with the optimal template matrix size (16 × 16) and sufficient number (300 or more) of initial local feature points would not be affected

substantially, except for cases where systemic changes have occurred, such as trauma in Figure 6a.

There are limitations associated with our study. Our method requires the following between prior and current scans: existing and parseable scout images, use of the same equipment, same image quality, and a time period that does not significantly affect the whole structure of the patient due to aging.

This study is a retrospective analysis performed on a single CT system with the same acquisition parameters. Another limitation is that our database has a short-term follow-up period of thirteen months. This is because 619 patients were scanned in the period of May 2015 to May 2016, and the effect of change in aging could not be evaluated in our study. Consequently, we have not evaluated long-term changes and the effect of using different CT systems. These limitations hindered the confirmation of our method's applicability in a wide range of sites.

If the CT system is different, several geometrical settings and digital values of the scout CT image also differ. Furthermore, with age, loss of calcium occurs in bones; thus, the digital value of the scout CT image is expected to decrease. In addition, the effect of changes in body habitus are also related to age (secular trend). However, as shown in Figure 7, our preliminary study using different CT systems

achieved a correspondence rate of 61.0%. We believe that this result was equivalent level to 58.7% for the same CT system, and also within the equivalent range of 65.4 ± 16.3% for an average correspondence rate for the same CT system. Hence, we believe that the geometrical correction of our methodology is applicable even if a patient is scanned with different CT systems. Moreover, it is assumed that age-related changes in the human skeletal structure have a negligible contribution to scout CT images. We believe that the local feature extraction, which mainly extracts the human skeletal structure, and the valid correspondence evaluation of our methodology are also minimally affected by the performance of our method, even with variations in acquisition parameters, body habitus, and aging.

Although repeated follow-up research is needed over longer time periods and with the use of a variety of scan conditions, we think that both age-related changes and acquiring a different CT system do not affect the performance of our method. Thus, we believe that our proposed method is a novel approach that can be applied in biological fingerprint analysis based on the use of scout CT patient images from the chest, abdomen, and pelvis.

5. Conclusions

In this study, we have proposed an innovative biological fingerprint technique using scout CT images that are easily available from routine chest, abdomen, and pelvis CT scans. Furthermore, it is possible to collect precise patient information and match individuals to their medical records without disrupting both patient convenience and the primary tasks of healthcare provider. We consider that our method for chest abdomen, and pelvis CT examinations will provide a key solution to prevent patient misidentification attributed to human errors.

6. Acknowledgments

This study was partly supported by JSPS KAKENHI (Grant number JP18K15590). The authors would like to thank Dr. Shohei Kudomi from Yamaguchi University Hospital, Japan, for his advice on improving our manuscript, and Editage [http://www.editage.com] for editing this manuscript for English language.

7. Conflicts of Interest

The authors have no relevant conflicts of interest to disclose.

8. References

1. Bittle MJ, Charache P, Wassilchalk DM. Registration-associated patient misidentification in an academic medical center: causes and corrections. Jt Comm J Qual Patient Saf. 2007;33(1):25-33. doi:10.1016/S1553-7250(07)33004-3

2. Danaher LA, Howells J, Holmes P, Scally P. Is it possible to eliminate patient identification errors in medical imaging? J Am Coll Radiol. 2011;8(8):568-574. doi:10.1016/j.jacr.2011.02.021.

3. Henneman PL, Fisher DL, Henneman EA, Pham TA, Campbell MM, Nathanson BH. Patient identification errors are common in a simulated setting. Ann Emerg Med. 2010;55(6):503-509. doi:10.1016/j.annemergmed.2009.11.017.

4. Schulmeister L. Patient misidentification in oncology care. Clin J Oncol Nurs. 2008;12(3):495-498. doi:10.1188/08.CJON.495-498.

5. Snyder ML, Carter A, Jenkins K, Fantz CR. Patient misidentifications caused by errors in standard bar code technology. Clin Chem. 2010;56(10):1554-1560. doi:10.1373/clinchem.2010.150094.

6. Medicine Io. To Err Is Human: Building a Safer Health System. Washington, DC: The National Academies Press; 2000. doi:10.17226/9728.

7. Bennardello F, Fidone C, Cabibbo S, Calabrese S, Garozzo G, Cassarino G, Antolino A, Tavolino G, Zisa N, Falla C, Drago G, Di Stefano G, Bonomo P. Use of an identification system based on biometric data for patients requiring transfusions guarantees transfusion safety and traceability. Blood Transfus. 2009;7(3):193-203. doi:10.2450/2009.0067-08.

8. An Introduction to Biometric Data Analysis. In: Dunstone T, Yager N, eds. Biometric System and Data Analysis: Design, Evaluation, and Data Mining. Boston, MA: Springer US; 2009:3-26. doi:10.1007/978-0-387-77627-9_1.

9. Newman R. Security and Access Control Using Biometric Technologies: Application, Technology, and Management. Course Technology Press; 2009.

10. Council NR. Biometric Recognition: Challenges and Opportunities. Washington, DC: The National Academies Press; 2010. doi:10.17226/12720.

11. Ueda Y, Morishita J, Kudomi S, Ueda K. Usefulness of biological fingerprint in magnetic resonance imaging for patient verification. Med Biol Eng Comput. 2016;54(9):1341-1351. doi:10.1007/s11517-015-1380-x.

12. Silverstein E, Snyder M. Implementation of facial recognition with Microsoft Kinect v2 sensor for patient verification. Med Phys. 2017;44(6):2391-2399. doi:10.1002/mp.12241.

13. Wiant DB, Verchick Q, Gates P, et al. A novel method for radiotherapy patient identification using surface imaging. J Appl Clin Med Phys. 2016;17(2):271-278. doi:10.1120/jacmp.v17i2.6066.

14. Jeon B, Jeong B, Jee S, Huang Y, Kim Y, Park GH, Kim J, Wufuer M, Jin X, Kim SW, Choi TH. A Facial Recognition Mobile App for Patient Safety and Biometric Identification: Design, Development, and Validation. JMIR Mhealth Uhealth. 2019;7(4):e11472. doi:10.2196/11472.

15. Parks CL, Monson KL. Automated facial recognition of computed tomography-derived facial images: patient privacy implications. J Digit Imaging. 2017;30(2):204–14. doi:10.1007/s10278-016-9932-7.

16. Belgacem N, Fournier R, Nait-Ali A, Bereksi-Reguig F. A novel biometric authentication approach using ECG and EMG signals. J Med Eng Technol. 2015;39(4):226-238. doi:10.3109/03091902.2015.1021429.

17. Jekova I, Krasteva V, Schmid R. Human Identification by Cross-Correlation and Pattern Matching of Personalized Heartbeat: Influence of ECG Leads and Reference Database Size. Sensors (Basel). 2018;18(2). doi:10.3390/s18020372.

18. Koike-Akino T, Mahajan R, Marks TK, et al. High-accuracy user identification using EEG biometrics. Conf Proc IEEE Eng Med Biol Soc. 2016;2016:854-858. doi:10.1109/EMBC.2016.7590835.

19. Morishita J, Katsuragawa S, Sasaki Y, Doi K. Potential usefulness of biological fingerprints in chest radiographs for automated patient recognition and identification. Acad Radiol. 2004;11(3):309-315. doi:10.1016/S1076-6332(03)00655-X

20. Shimizu Y, Matsunobu Y, Morishita J. Evaluation of the usefulness of modified biological fingerprints in chest radiographs for patient recognition and identification. Radiol Phys Technol. 2016;9(2):240-4. doi:10.1007/s12194-016-0355-4.

21. Shimizu Y, Morishita J. Development of a method of automated extraction of biological fingerprints from chest radiographs as preprocessing of patient recognition and identification. Radiol Phys Technol. 2017;10(3):376-381. doi:10.1007/s12194-017-0400-y.

22. Kao EF, Lin WC, Jaw TS, Liu GC, Wu JS, Lee CN. Automated patient identity recognition by analysis of chest radiograph features. Acad Radiol. 2013;20(8):1024-31. doi:10.1016/j.acra.2013.04.006.

23. Shamir L, Ling S, Rahimi S, Ferrucci L, Goldberg IG. Biometric identification using knee X-rays. Int J Biom. 2009;1(3):365-370. doi:10.1504/IJBM.2009.024279.

24. Lamb JM, Agazaryan N, Low DA. Automated patient identification and localization error detection using 2-dimensional to 3-dimensional registration of kilovoltage x-ray setup images. Int J Radiat Oncol Biol Phys. 2013;87(2):390-3. doi:10.1016/j.ijrobp.2013.05.021.

25. Morishita J, Katsuragawa S, Kondo K, Doi K. An automated patient recognition method based on an image-matching technique using previous chest radiographs in the picture archiving and communication system environment. Med Phys. 2001;28(6):1093-1097. doi:10.1118/1.1373403.

26. Morishita J, Watanabe H, Katsuragawa S, et al. Investigation of misfiled cases in the PACS environment and a solution to prevent filing errors for chest radiographs. Acad Radiol. 2005;12(1):97-103. doi:10.1016/j.acra.2004.11.008.

27. Toge R, Morishita J, Sasaki Y, Doi K. Computerized image-searching method for finding correct patients for misfiled chest radiographs in a PACS server by use of biological fingerprints. Radiol Phys Technol. 2013;6(2):437-43. doi:10.1007/s12194-013-0221-6.

28. ISO. ISO/IEC 19795-1:2006 Information technology - Biometric Performance Testing and Reporting - Part 1: Principles and Framework; 2006.

29. Vincent L, Dougherty ER. Morphological segmentation for textures and particles. In: Dougherty ER (Ed.), Digital Image Processing Methods, Marcel Dekker, New York. 1994:43-102.

30. Briechle K, Hanebeck UD. Template matching using fast normalized cross correlation. Proc. SPIE, vol. 4387, pp. 95-102, 2001. doi: 10.1117/12.421129.

31. DeLong ER, DeLong DM, Clarke-Pearson DL. Comparing the areas under two or more correlated receiver operating characteristic curves: a nonparametric approach. Biometrics. 1988;44(3):837-45. doi:10.2307/2531595.

32. Robin X, Turck N, Hainard A, Tiberti N, Lisacek F, Sanchez JC, Müller M. pROC: an open-source package for R and S+ to analyze and compare ROC curves. BMC Bioinformatics. 2011;12:77. doi:10.1186/1471-2105-12-77.

Figure Legends

Figure 1 Scan geometry of the chest-abdomen-pelvis scout CT scan. Scout CT images are acquired with the patient in the supine position with his/her arms raised above his/her head. The couch is translated at constant speed through the gantry opening during X-ray acquisition. The X-ray tube and detector array do not rotate around the patient during scout image acquisition. D_{SO}: distance from the focal spot in the X-ray tube to the rotation center, table height (TH): distance from couch to the rotation center.

Figure 2 Flowchart of our biological fingerprint verification framework. The biological fingerprint verification process is executed using four major steps: a) geometric correction, b) local feature extraction, c) valid correspondence evaluation, and d) similarity evaluation. The correspondence rate, C, is the similarity index.

Figure 3 Image examples of geometric correction and local feature extraction based on the variation of the top N peaks of local maxima. (a-d) A patient's scout image without any metal artifacts: (a) Original image and (b-d) cropped processing areas of the geometrically corrected images. Yellow circles represent the initial local feature points in the processing area by varying the (b) top-100 peaks, (c) top-200 peaks, and (d) top-300 peaks of the local maxima. (e-h) A patient's scout image with metal artifacts (residual contrast medium in the gastrointestinal tract): (e) Original image and (f-h) cropped processing areas of the geometrically corrected images. Yellow circles represent the initial local feature points in the processing area by varying the (f) top-100 peaks, (g) top-200 peaks, and (h) top-300 peaks of the local maxima.

Figure 4 Example images of genuine and impostor pair analyses at N = 300, X = Y = 16. A follow-up scan (center) and a baseline scan (right) correspond to the same patient pair. All images are cropped to select the processing area and are geometrically corrected. A follow-up (center) and baseline (left) scans correspond to a different patient pair. Yellow circles indicate the initial local feature points in the follow-up scan and the local corresponding points in the baseline scan. Lines connecting pairs of yellow circles in pairs of images are valid corresponding feature points on the genuine pair (cyan lines) and impostor pair (magenta lines). The correspondence rates achieved are 80.6% for the genuine pair and 18.0% for the

impostor pair. (N denotes the number of the initial local feature points, and X and Y denote the rows and columns of the template matrix size, respectively).

Figure 5 Example demonstrating an increased correspondence rate in an impostor pair evaluation at N = 300, X = Y = 16. Follow-up (right) and baseline scans (left) from different patients. Both images have been geometrically corrected. Yellow circles denote the sets of the initial local feature points in the follow-up scan and the local corresponding points in the baseline scan. Magenta lines connecting pairs of yellow circles in the two scans denote valid corresponding feature points. The correspondence rate achieved is 44.3%. (N denotes the number of initial local feature points, and X and Y denote the rows and columns of the template matrix size, respectively).

Figure 6 Example demonstrating low correspondence rate examples for a genuine pair evaluation at N = 300, X = Y = 16. Example demonstrating low correspondence rate examples due to a) translocations in the patient's body posture and b) a patient with metal artifacts (residual contrast medium in the gastrointestinal tract). Follow-up (right) and baseline (left) scans of single patients. Both images have been geometrically corrected. Yellow circles denote the initial local feature points in the follow-up scan and the local corresponding points in the baseline scan. Cyan lines connecting pairs of yellow circles in the two scans denote valid corresponding feature points. The correspondence rates we achieved are a) 15.0% and b) 33.3%, respectively. (N denotes the number of initial local feature points, and X and Y denote the rows and columns of the template matrix size, respectively).

Figure 7 Example images for analyses of same and different CT systems at N = 300, X = Y = 16. All three scout CT images are for the same patient and cropped to select the processing area and have been geometrically corrected. A follow-up (center) and a baseline (right) scan are acquired from the single CT system (SOMATOM Sensation 64, Siemens Medical Solutions, Forchheim, Germany). However, only a baseline (left) scan is acquired from different CT system (SOMATOM Definition, Siemens Medical Solutions, Forchheim, Germany). Yellow circles indicate the initial local feature points in the follow-up scan and the local corresponding points in the baseline scan. Lines connecting pairs of yellow circles in pairs of images denote valid corresponding feature points on the same CT system (cyan lines) and a different CT system (green lines). The correspondence rates achieved are 58.7% for the same CT

system and 61.0% for a different CT system. (N denotes the number of the initial local feature points, and X and Y denote the rows and columns of the template matrix size, respectively).

Figure 8 Comparison of ROC curve performances for four template matrix sizes at N = 300. The plotted ROC curves correspond to template matrix sizes of 8 × 8 (green line), 16 × 16 (red line), 32 × 32 (blue line), and 64 × 64 (black line). N indicates the number of initial local feature points.

Figure 9 Comparison of CMC curve performances for four template matrix sizes at N = 300. The plotted CMC curves correspond to template matrix sizes of 8 × 8 (green line), 16 × 16 (red line), 32 × 32 (blue line), and 64 × 64 (black line). N indicates the number of initial local feature points.

Figure 10 Comparison of performance values by varying the number of initial local feature points for four template matrix sizes. (a) Variations of EER for the template matrix sizes of 8 × 8 (green line), 16 × 16 (red line), 32 × 32 (blue line), and 64 × 64 (black line) as a function of the number of initial local feature points. (b) Variations of R1 for the template matrix sizes of 8 × 8 (green line), 16 × 16 (red line), 32 × 32 (blue line), and 64 × 64 (black line) as a function of the number of initial local feature points.

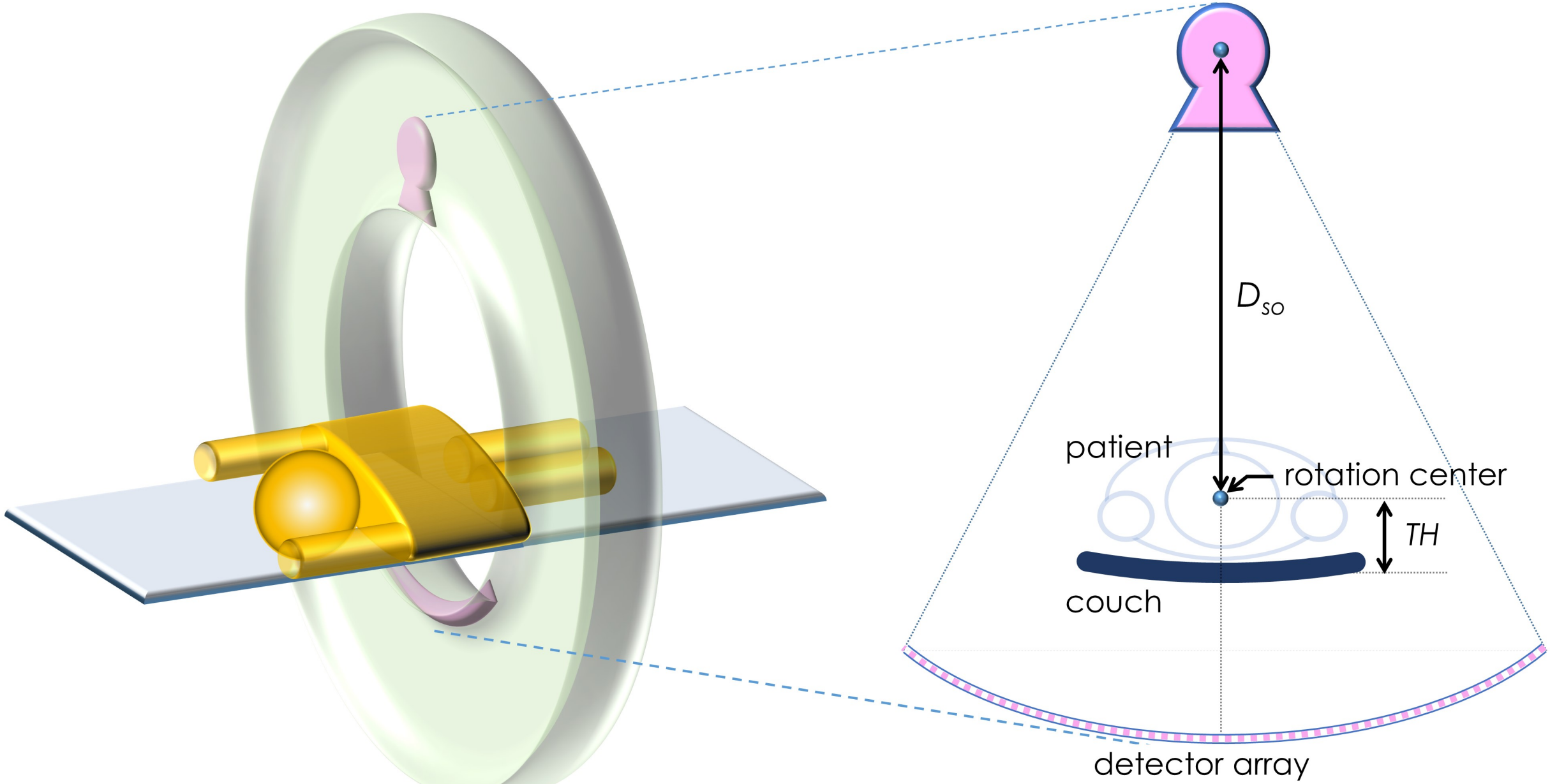
X-ray tube
D_{SO}
patient
rotation center
TH
couch
detector array

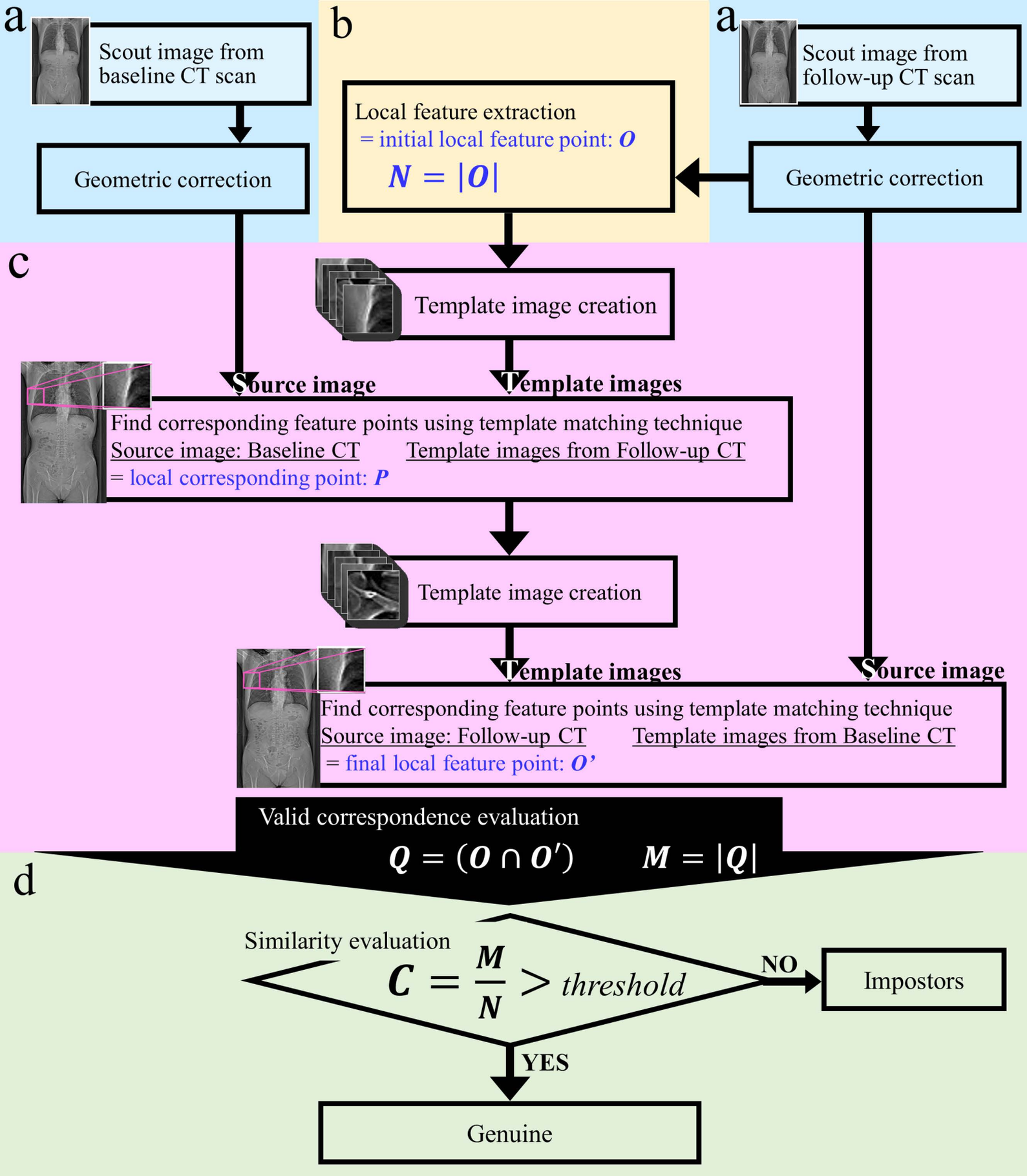

O	: initial local feature point (on the follow-up scout CT image)	
N	: number of initial local feature point ----------	$N = \|O\|$
P	: local corresponding point (on the baseline scout CT image)	
O'	: final local feature point (on the follow-up scout CT image)	
Q	: valid corresponding feature point ----------	$Q = (O \cap O')$
M	: number of valid corresponding feature point ----------	$M = \|Q\|$
C	: correspondence rate ----------	$C = M/N$

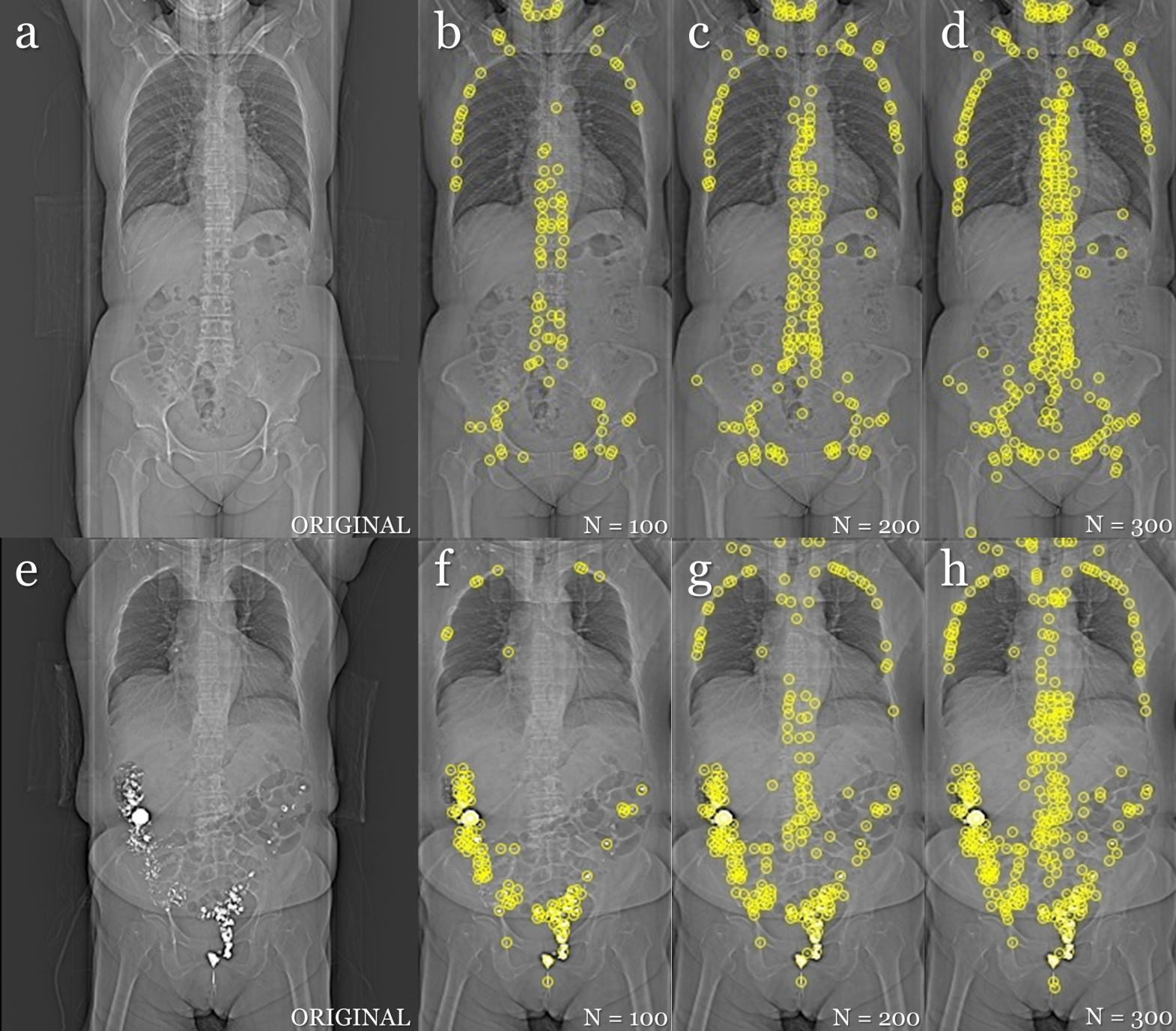
a
b
c
d
ORIGINAL
N = 100
N = 200
N = 300
e
f
g
h
ORIGINAL
N = 100
N = 200
N = 300

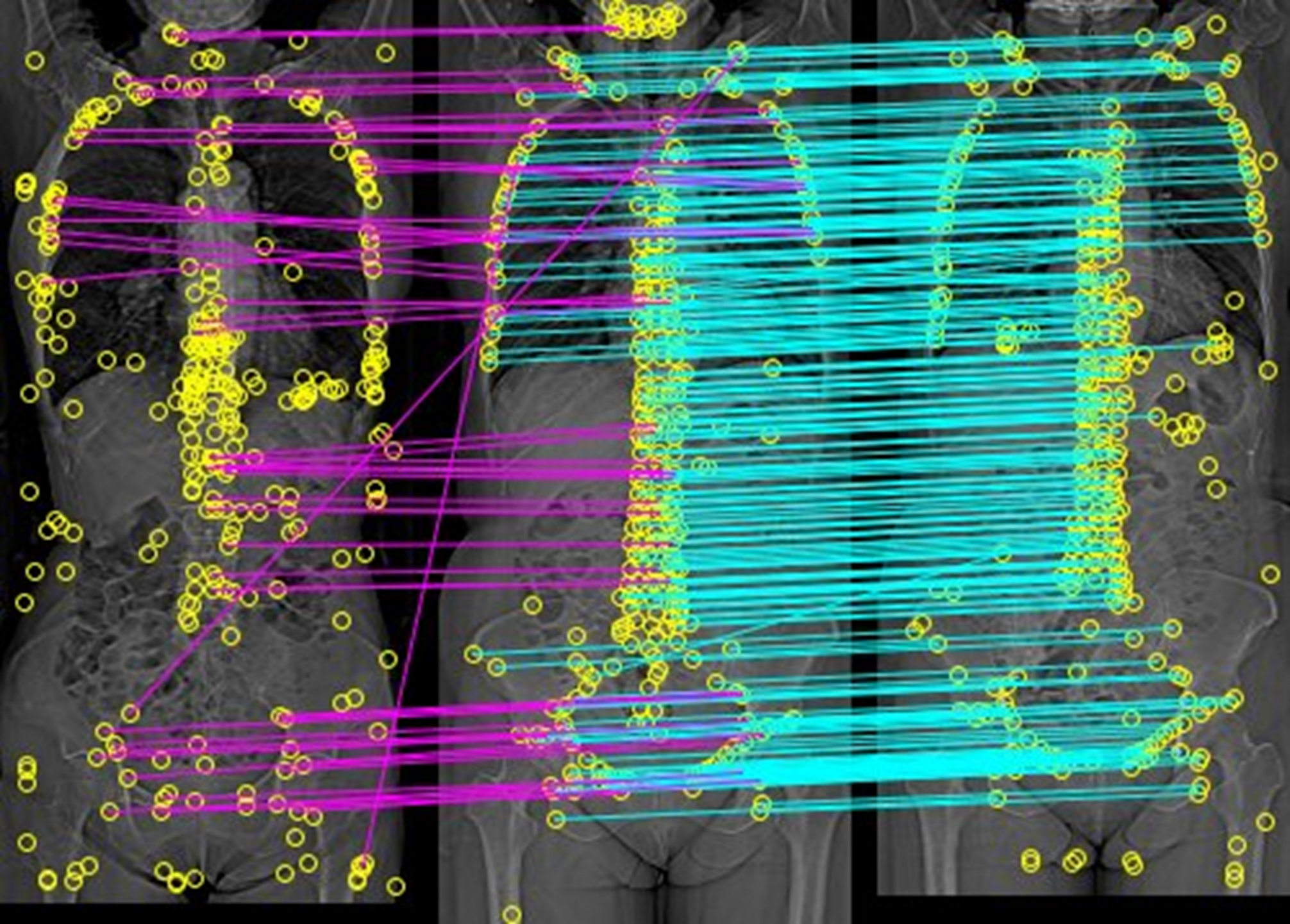

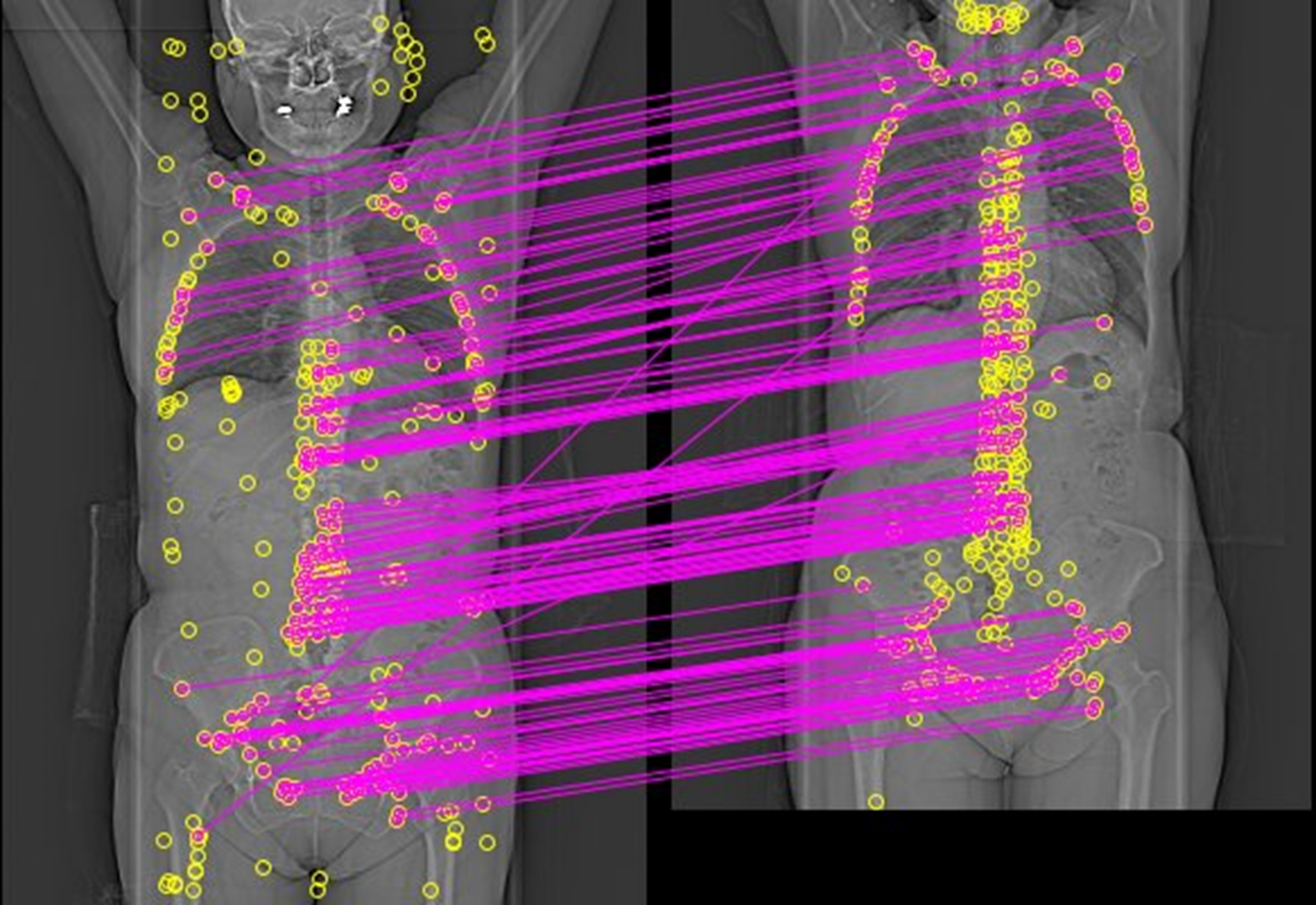

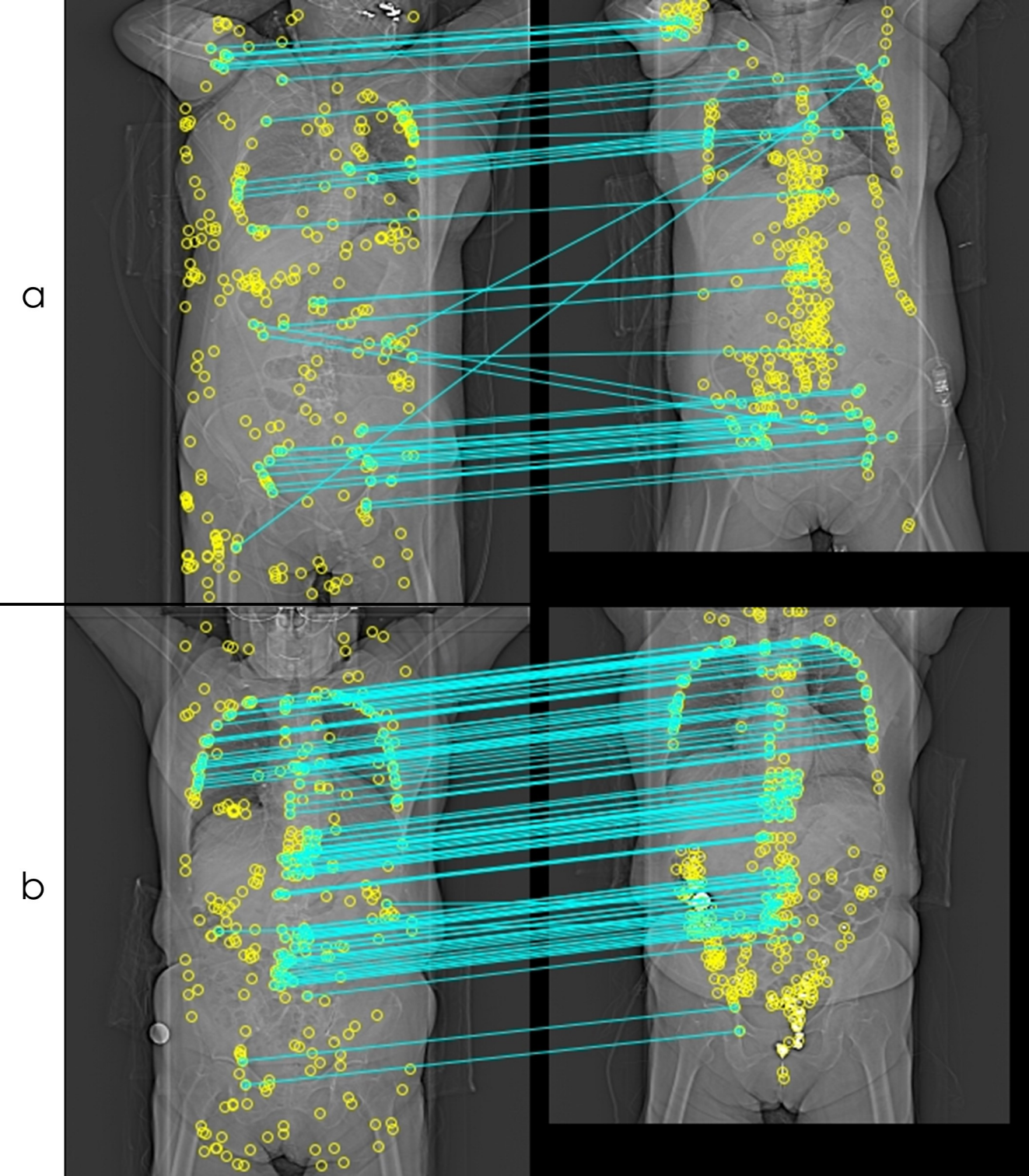
a
b

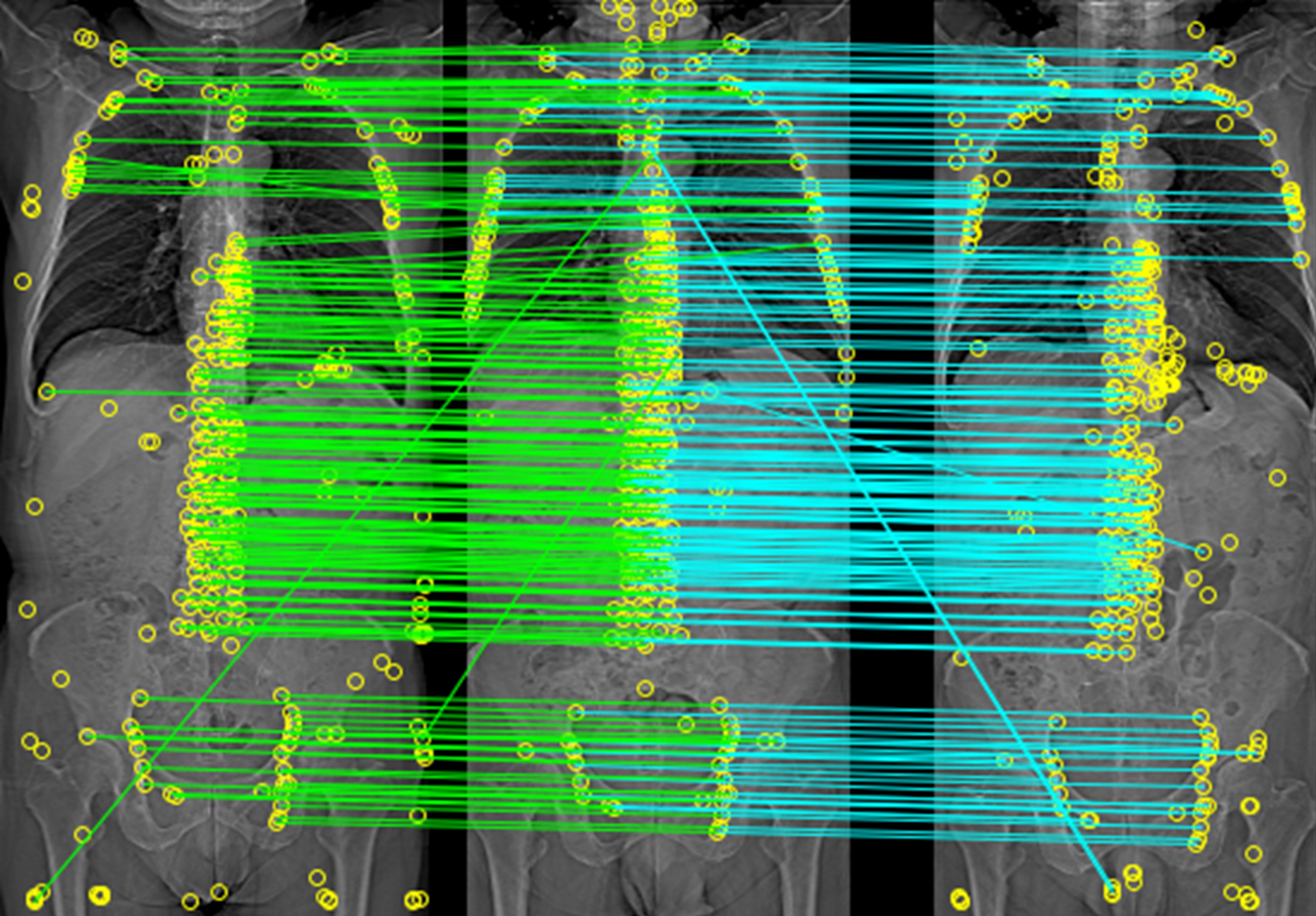

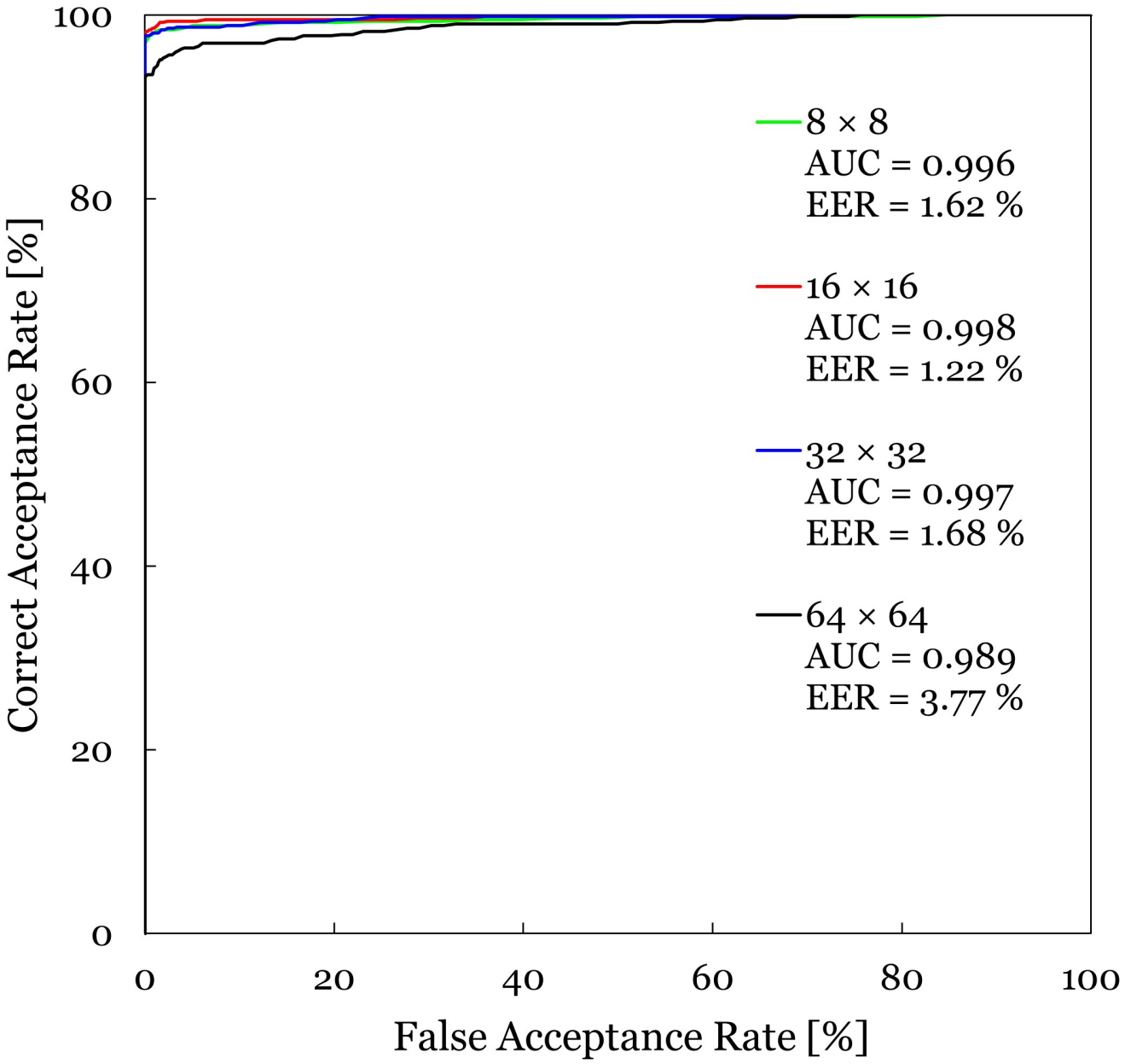
100
80
60
40
20
0
Correct Acceptance Rate [%]
0
20
40
60
80
100
False Acceptance Rate [%]
8 × 8
AUC = 0.996
EER = 1.62 %
16 × 16
AUC = 0.998
EER = 1.22 %
32 × 32
AUC = 0.997
EER = 1.68 %
64 × 64
AUC = 0.989
EER = 3.77 %

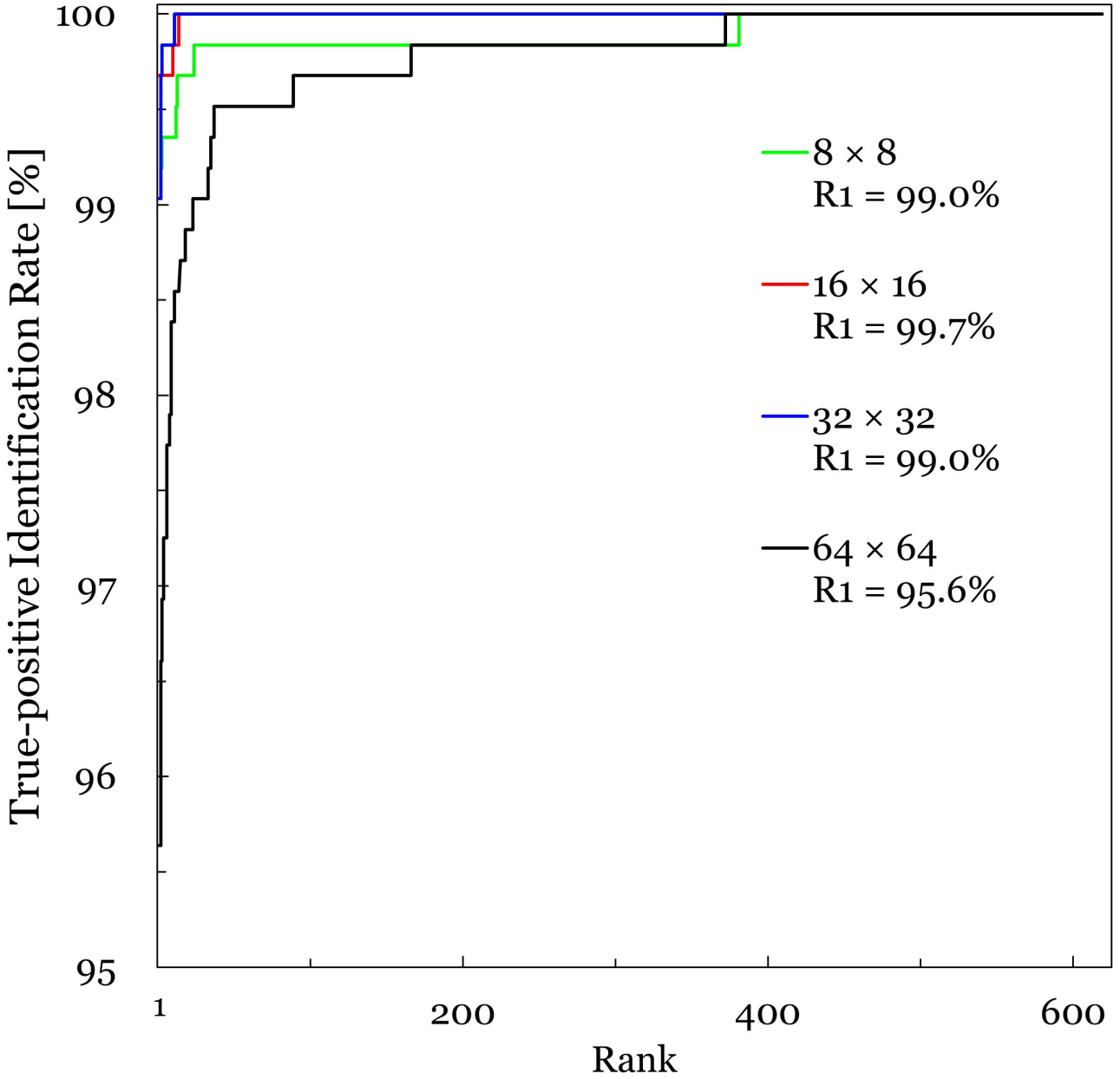
100
99
98
97
96
95
True-positive Identification Rate [%]
1
200
400
600
Rank
8 × 8
R1 = 99.0%
16 × 16
R1 = 99.7%
32 × 32
R1 = 99.0%
64 × 64
R1 = 95.6%

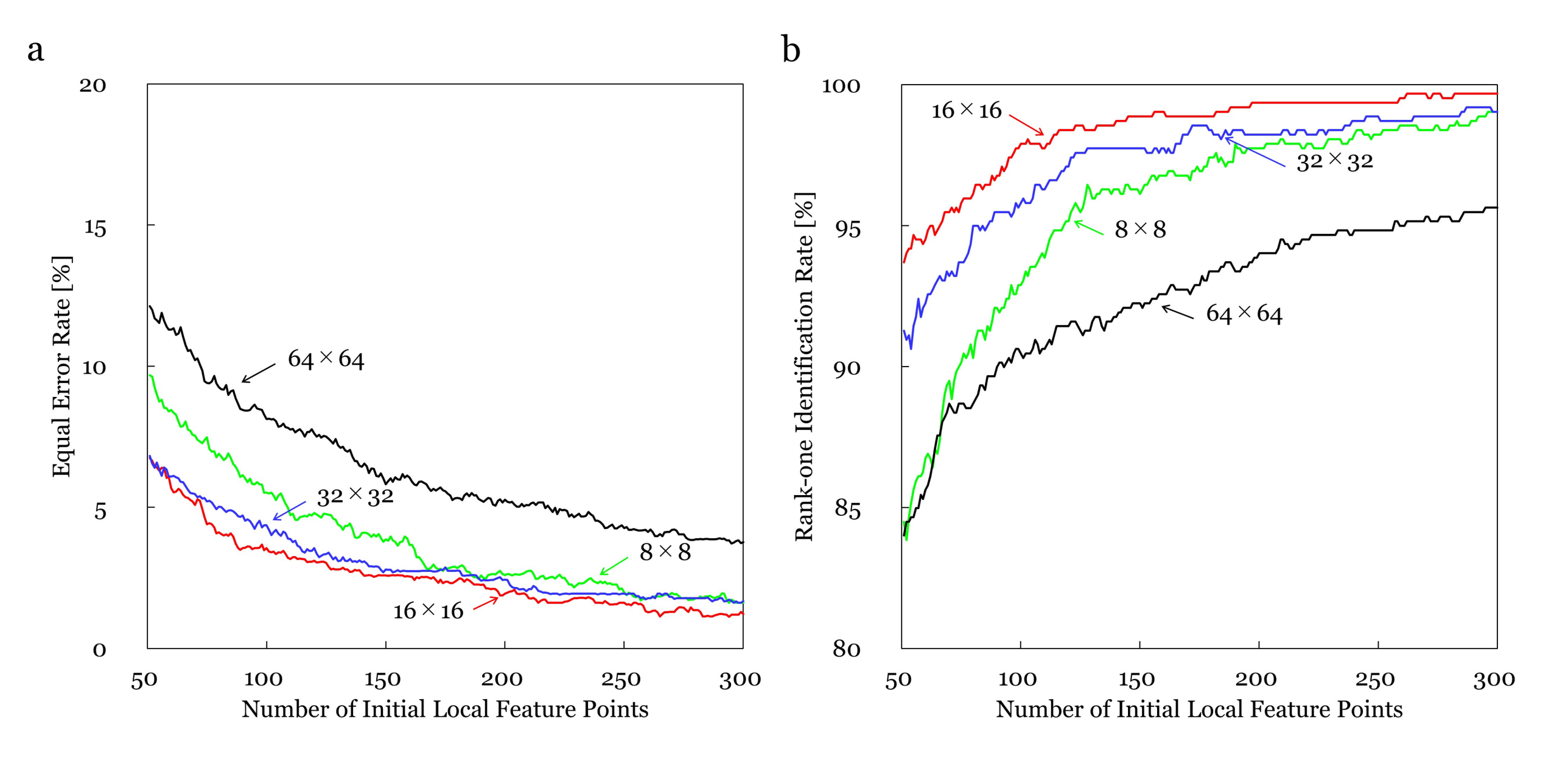
a
Equal Error Rate [%]
20
15
10
5
0
50
100
150
200
250
300
Number of Initial Local Feature Points
64 × 64
32 × 32
8 × 8
16 × 16
b
Rank-one Identification Rate [%]
100
95
90
85
80
50
100
150
200
250
300
Number of Initial Local Feature Points
16 × 16
32 × 32
8 × 8
64 × 64

Table I Patient characteristics

Number of patients	619	
Age		
mean ± standard deviation	67 ± 12	years
Range	21 – 92	years
Sex		
Male	383	
Female	286	
scan intervals between the baseline and follow-up examinations		
within 1 week	28	
from 1 week to 1 month	65	
from 1 to 3 months	143	
from 3 to 6 months	236	
from 6 months to 1 year	147	
Table height of scout CT image		
mean ± standard deviation	147 ± 13	mm
Range	111 - 209	mm
Type of artifact including follow-up scout image		
None	364	(299)
Include metal artifact	255	(117)
inside their body	210	(109)
outside their body	30	(7)
Both inside and outside their body	15	(1)

Numbers in parentheses indicate the numbers of artifacts in both the baseline and follow-up scout images.

Table I Scan parameters

Tube voltage	120	kV
Tube current	35	mA
Physical width of the image measured at the rotation center		
Detector size	0.6	mm
Field of view	560	mm

Table I Evaluation of the ROC performance classified by whether the scout CT image includes metal artifacts or not in the follow-up CT scan by varying the number of initial local feature points and template matrix sizes

template matrix size		8 × 8	16 × 16			32 × 32	64 × 64
number of initial local feature points		300	100	200	300	300	300
AUC	with metal artifacts (255)	0.996	0.981	0.980	0.998	0.998	0.986
	without metal artifacts (364)	0.993	0.996	0.996	0.999	0.999	0.993
p-value		0.393	0.0206*	0.0199*	0.488	0.612	0.209

Numbers in parentheses indicate the numbers of patients in each group. Asterisks (*) indicate a statistically significant ($p < 0.05$) difference in unpaired Delong's test depending on whether a metal artifact was present.